Journal of the European Ceramic Society 45 (2025) 117277

Contents lists available at ScienceDirect

Journal of the European Ceramic Society

journal homepage: www.elsevier.com/locate/jeurceramsoc

From individual to equimolar binary transition metal diborides: The case of $(Nb_{0.5}M_{0.5})B_2$, M=Ti, Hf

Luca Cappai [a], Mariano Casu [a], Antonio Mario Locci [a], Giacomo Cao [a], Sebastiano Garroni [b], Valeria Cannillo [c], Devis Bellucci [c], Roberto Orrù [a,*]

[a] Dipartimento di Ingegneria Meccanica, Chimica e dei Materiali, Unità di Ricerca del Consorzio Interuniversitario Nazionale per la Scienza e Tecnologia dei Materiali (INSTM), Università degli Studi di Cagliari, Via Marengo 2, Cagliari 09123, Italy
[b] Dipartimento di Scienze Chimiche, Fisiche, Matematiche e Naturali, Università degli Studi di Sassari, Via Vienna 2, Sassari 07100 , Italy
[c] Dipartimento di Ingegneria "Enzo Ferrari", Università di Modena e Reggio Emilia, Via P. Vivarelli 10, Modena 41125, Italy

ARTICLE INFO

Keywords:
Solid solution
Borides
Spark plasma sintering
Self-propagating High-temperature synthesis
Resistance to oxidation

ABSTRACT

$(Nb_{0.5}Ti_{0.5})B_2$ and $(Nb_{0.5}Hf_{0.5})B_2$ in bulk form were produced by Spark Plasma Sintering (SPS) from powders obtained by Self-propagating High-temperature Synthesis. The carbothermal reduction of oxide contaminants with graphite promoted the conversion of secondary phases into equimolar diborides, and improved samples densification, particularly for $(Nb_{0.5}Hf_{0.5})B_2$ (from 89.7 % to 97.4 %). A single-phase solid solution was obtained for both systems at 2050 °C by SPS, while longer holding times (40 instead of 20 min) were needed for the Hf-containing ceramic. The latter system showed Vickers hardness (18.47 GPa) and Young's modulus (586 GPa) slightly better than HfB_2. NbB_2 and $(Nb_{0.5}Hf_{0.5})B_2$ were the most sensitive systems to the oxidation environment, with the formed oxide scales detached from samples at 600 and 800 °C, respectively, due to volume changes accompanying phase transitions in the generated niobium oxides. Conversely, the formation of a stable mixed oxide ($TiNb_2O_7$) made $(Nb_{0.5}Ti_{0.5})B_2$ more resistant to oxidation, compared to TiB_2 and NbB_2.

1. Introduction

Their high melting points and other exclusive physical-chemical properties make Ultra High Temperature Ceramics (UHTCs) based on transition metal diborides very suitable for structural applications under severe environmental conditions [1,2]. Such interest prompted the scientific community to investigate them in detail, first by focusing on individual systems (MB_2, with M=Zr, Hf, Ta, Nb, etc.) while, in the last decade, various multicomponent ceramics, in particular quinary High Entropy Borides (HEBs), have been considered [3–11].

In this framework, ZrB_2-, HfB_2-, and TiB_2-based UHTCs are the most investigated diboride ceramics [1,2], although studies have been also addressed to the fabrication and characterization of NbB_2 [12–16]. The latter system is also one of the base constituents often involved in the various HEBs investigated so far [3–11]. In particular, the effect of the Nb content on the densification behavior, composition, microstructure and mechanical properties of $(Hf,Zr,Ti,Ta,Nb)B_2$ ceramics was investigated by Feng et al. [11]. Only a fraction of the Nb added was observed to dissolve into the main HEB phase, while a Nb-rich secondary phase was also formed in all the compositions investigated. The presence of the latter phase was considered responsible for the reduction of grain size (from 13.9 ±5.5 to 5.2 ±2.0 μm, as the Nb content increased from 0 to 20 at%), and the corresponding increase of Vickers hardness and Young's modulus properties. More recently, the oxidation resistance of ZrB_2 ceramics was improved after covering their surface with metallic Nb-coatings by means of magnetron sputtering [17]. This outcome was explained by the increased stability of the protective glass at the ceramic surface caused by liquid Nb_2O_5 formed during the oxidation test.

Despite the potential benefits deriving by the use of Niobium, only a little attention has been paid so far to two-components (transition metals) systems, hereafter also named as binary diborides, containing this element. For instance, to the best of our knowledge, the obtainment of $(Nb_xHf_{1-x})B_2$ has been considered only in two recent studies, where controversial results are reported [18,19]. Specifically, the preparation of $(Nb_{0.9}Hf_{0.1})B_2$, $(Nb_{0.5}Hf_{0.5})B_2$, and $(Nb_{0.1}Hf_{0.9})B_2$ powders failed when using the high throughput molten salt synthesis method [18]. Such experimental findings agree with theoretical results provided by the formation criterion developed by the same authors. A different

* Corresponding author.
E-mail address: roberto.orru@unica.it (R. Orrù).

https://doi.org/10.1016/j.jeurceramsoc.2025.117277
Received 27 October 2024; Received in revised form 2 February 2025; Accepted 9 February 2025
Available online 11 February 2025

outcome arose from Kurbatkina et al. [19], who were able to obtain $(Nb_{0.2}Hf_{0.8})B_2$, $(Nb_{0.4}Hf_{0.6})B_2$, and $(Nb_{0.5}Hf_{0.5})B_2$ samples in bulk form by Hot Pressing (HP) using powders previously prepared by Self-propagating High-temperature Synthesis (SHS). The latter processing step was preceded by a 12 h duration ball milling treatment (ball-to-powder weight ratio, BPR=6) of initial Nb, Hf, and B reactants. XRD analysis revealed that the sintered samples mainly consisted of the desired solid solutions with minor secondary phases (unidentified).

Analogously, only very few studies have been dedicated to the $(Nb_xTi_{1-x})B_2$ system [18,20,21]. Specifically, Demirskyi et al. [20] investigated the $(Nb_{2/3}Ti_{1/3})B_2$, $(Nb_{0.5}Ti_{0.5})B_2$, and $(Nb_{1/3}Ti_{2/3})B_2$ formulations using TiB_2, and NbB_2 as precursors. A multistep Spark Plasma Sintering (SPS) approach was applied and, depending on the processing conditions adopted, either (Nb,Ti)B_2 solid solutions or two-phase composites consisting of TiB_2 and NbB_2 were obtained. The high throughput molten salt synthesis method mentioned previously was also employed by Wen et al. [18] for the preparation of $(Nb_xTi_{1-x})B_2$ powders with different composition (x = 0.1, 0.5, 0.7, 0.8, 0.9). While $(Nb_{0.9}Ti_{0.1})B_2$, and $(Nb_{0.8}Ti_{0.2})B_2$ were synthesized as single-phase products, multiple phases resulted when considering the other three compositions. As for the case of (Nb,Hf)B_2, the experimental outcomes obtained with (Nb,Ti)B_2 were supported by the formation criterion proposed by the authors. More recently, and in contrast to Wen et al. [18], the synthesis of $(Nb_{0.75}Ti_{0.25})B_2$, $(Nb_{0.5}Ti_{0.5})B_2$, and $(Nb_{0.25}Ti_{0.75})B_2$ was successfully accomplished at 1850 °C by SPS from TiB_2 and NbB_2 powders [21]. The resulting sintered samples, with relative densities of 95.4 (x = 0.75), 97.5 (x = 0.5) and 98.6 % (x = 0.25), consisted of the expected solid solutions.

Based on the studies conducted so far, few and contradictory results are available regarding the possibility of synthesizing $(Nb_xHf_{1-x})B_2$ and $(Nb_xTi_{1-x})B_2$ solid solutions. In addition, the characterization of the produced ceramics was rather incomplete. For instance, the oxidation behavior of (Nb,Hf)B_2 is totally unexplored. As for the (Nb,Ti)B_2 system, oxidation tests have been carried out by Kaplan Akarsu et al. [21] only for the $(Nb_{0.25}Ti_{0.75})B_2$ composition, while no results are available for the equimolar and other formulations.

This situation opens the door for additional and more comprehensive studies on these ceramics, which will be able to provide a valuable contribution to fill such gap. As for their synthesis, benefits could be obtained using the two-step SHS-SPS approach, which was recently employed with success for the fabrication of dense and single-phase $(Zr_{0.5}Hf_{0.5})B_2$ and $(Zr_{0.5}Ta_{0.5})B_2$ [22,23] as well as quinary diborides [7,8,24,25]. The powders preliminarily synthesized during the SHS step generally consisted of multiple phases. However, the expected solid solutions were formed, with neither residual reactants nor secondary boride phases, during the subsequent SPS stage conducted under appropriate operating conditions.

Along this line, bulk $(Nb_{0.5}Hf_{0.5})B_2$ and $(Nb_{0.5}Ti_{0.5})B_2$ solid solutions are prepared in this work by SHS-SPS. In particular, this study focuses on the influence of the holding temperature and dwelling time on the composition and density of the two binary diboride products. The other operating parameters, in particular the applied pressure and heating rate, also affecting the SPS process and the characteristics of resulting ceramics [26,27] are kept constant. In addition, following the beneficial effect observed in previous studies (oxide impurities removal, improved powders reactivity and densification) when small amounts of graphite were added to the SHS powders before SPS [7,8,22,23,25], such a reducing agent is also employed in the present investigation.

Optimal bulk ceramics are exposed to flowing and stagnant air at high temperatures to provide a preliminary indication of their oxidation behavior under such conditions. Hardness, Young's modulus and fracture toughness properties are also measured. For the sake of comparison, individual diboride (NbB_2, HfB_2, and TiB_2) samples are also produced by SHS-SPS and properly characterized.

2. Experimental section

2.1. Powder synthesis and sintering

Commercial Nb (Alfa Aesar, < 44 μm, 99.8 % purity), Hf (Alfa Aesar, < 44 μm, 99.6 % purity), Ti (Thermo scientific, < 44 μm, 99 % purity), and B (amorphous, Sigma Aldrich, ≥ 95 % purity) powders were used as starting materials for the preparation of metal diborides. NB, TB, HB, NTB, and NHB abbreviations indicate samples obtained either by SHS or SPS when considering NbB_2, TiB_2, HfB_2, $(Nb_{0.5}Ti_{0.5})B_2$, and $(Nb_{0.5}Hf_{0.5})B_2$ systems, respectively.

As reported in previous works [7], where the synthesis of other diborides was accomplished using the same route, an excess of B (B/Me=2.2) was utilized to consider the presence of metal oxides, B_2O_3 and boric acid impurities in raw powders, and compensate for losses of this reactant generally occurring during the SHS step. Elemental precursors were mixed for 20 min (BPR=0.2) using a SPEX 8000 (SPEX CertiPrep, USA) shaker mill device, plastic vials, and agata balls. Mixtures were cold-pressed, and the obtained cylindrical pellets reacted into the SHS chamber, first evacuated and then filled with Argon, using an electrically heated tungsten filament to initiate the reaction. Synthesis products were ball milled for 1 h (SPEX CertiPrep, USA, BPR= 2, hardened steel vial and balls) without or in presence of 1 wt% graphite (Sigma-Aldrich, < 20 μm) to obtain powders for Spark Plasma Sintering experiments.

Proper amounts (from 2.3 to 5.7 g, depending on the system) of these powders were loaded into a hollow cylinder (30 mm external diameter; 15 mm inside diameter; 30 mm height) equipped with two punches (14.7 mm diameter, 20 mm height), all made of AT101 graphite (ATAL Srl., Italy). Powders were then processed under vacuum conditions (20 Pa) by SPS (515S model, Fuji Electronic Industrial Co., Ltd., Kanagawa, Japan) following a prescribed thermal cycle, where temperature was measured by an infrared pyrometer (CHINO, mod. IR-AHS2, Japan) focused on the lateral surface of the die. The dwell temperature (T_D) and holding time (t_D) values to produce the bulk samples were varied, depending on the system, in the range 1850–2050 °C and 10–40 min, respectively. Higher temperature levels and longer dwelling times were not applicable due to the limitations of the SPS apparatus used in this work. The heating rate and applied pressure were maintained the same, 200 °C/min, and 20 MPa, respectively. For the sake of reproducibility, each experiment was repeated at least twice. Before characterization, SPS samples were properly ground and polished to remove residual graphite.

2.2. Compositional and structural characterization

Particle size of SHS powders after the ball milling treatment was measured by laser light scattering analysis (CILAS 1180, France).

Phases identification and microstructural characteristics of the synthesized powders and sintered products was performed by X-ray diffraction analysis using a SMARTLAB diffractometer with a rotating anode source of copper (λCu Kα = 1.54178 Å) working at 40 kV and 100 mA over a range of scattering angles 2ϑ from 20 to 130, in steps of 0.05° with 15 s acquisition time per angle. Phases amount (wt%) and related structural parameters were evaluated with the Rietveld method by analyzing the XRD patterns with the MAUD program [28]. For the estimation of crystallite size and microstrain, the isotropic model was applied. Regarding the line broadening, a pseudo-Voigt function was employed.

Microstructure and elemental distribution of SHS and SPS products were investigated by high-resolution scanning electron microscopy (HR-SEM, mod. S4000, Hitachi, Tokyo, Japan) equipped with a UltraDry EDS detector (Thermo Fisher Scientific, Waltham, MA, USA).

Samples density was determined by the Archimedes' method, using distilled water as immersing medium. The theoretical values of 6.97 [29], 4.50 [30], 11.21 g/cm^3 [29], were used for NbB_2, TiB_2, and HfB_2,

respectively, to calculate the corresponding relative densities. The values (ρ_c) of 5.77 and 9.11 g/cm^3 for $(Nb_{0.5}Ti_{0.5})B_2$, and $(Nb_{0.5}Hf_{0.5})B_2$, respectively, were estimated according to related lattice parameters from CIF files (COD-1510775 and COD-1510708) by using the following formula:

$$\rho_c = (Z \cdot M/V_c) \cdot (10^{24}/N_A)$$

where Z is the stoichiometry of each element, M the corresponding molar mass, V_c the volume of the lattice cell, and N_A the Avogadro constant [22].

2.3. Mechanical properties

The micro-indentation technique was used to evaluate the hardness and Young's modulus of the samples. Testing was carried out with the Open Platform system (CSM Instruments, Peseux, Switzerland), utilizing a Vickers indenter tip. A 3 N load was applied, with a loading/unloading rate of 6 N/min, and the maximum load was held for 15 seconds. For each sample, a minimum of 15 measurements were taken, and the load-penetration depth curve was automatically recorded for each indentation. The elastic modulus was then calculated using the Oliver and Pharr method, based on the load-unloading curves [31]. Fracture toughness was also assessed by applying a 5 N load to generate crack propagation from the indent tips; the loading/unloading rate was 10 N/min. The toughness was calculated from the crack lengths using well-established equations from the literature [32,33].

2.4. Oxidation behaviour

The oxidation resistance of optimal sintered products was evaluated in air by thermogravimetric analysis (NETZSCH, STA 409PC Luxx Simultaneous DTA-TGA Instrument, Germany) as well as using a muffle furnace (LT 24/11/B410, Nabertherm, Lilienthal, Germany). Non-isothermal (dynamic) TGA tests were conducted from room temperature to 1450 °C (2 °C/min) and 0.1 L/min air flow. Furnace experiments consisted in heating the specimens in stagnant air at a rate of 4 °C/min from room temperature to a maximum value, in the range of 600–1200 °C, followed by an isothermal step of 1 h duration. The resulting samples were examined by XRD (Bruker D8 Advance diffractometer, copper source λCu Kα = 1.54178 Å, working at 40 kV and 40 mA over a range of scattering angles 2θ from 20° to 130°, in steps of 0.05° with 5 s acquisition time per angle) and SEM/EDS.

3. Results and discussion

3.1. Individual diborides

According to the high enthalpy of formation of the three individual diborides from their elements, i.e −251.040 (NbB_2), −323.800 (TiB_2), −335.975 kJ/mol (HfB_2) [34], the related mixtures exhibit, upon ignition, a self-propagating character. The measured average velocities were about 2, 9, and 8 mm/s, respectively. The slower propagation front observed when reacting the NB mixture is in accordance with the relatively lower heat of formation of NbB_2.

As shown in Figs. 1a-3a, where the XRD patterns of the resulting products are reported, elemental reactants are almost completely converted during SHS into the expected hexagonal phases. Indeed, while no other phases were detected by XRD analysis on NB powders, only low amounts of $TiBO_3$ (~1.6 wt%), and HfO_2 (~0.6 wt%), were found in TB and HB samples, respectively (supplementary Tables S1-S3). The crystallite size of the diboride products in the ball milled SHS powders, also estimated by the Rietveld analysis, was at the nanoscale, i.e. about 53 (NbB_2), 88 (TiB_2), and 52 nm (HfB_2).

The three batches of powders were also examined by SEM and EDS analysis (Figures S1a-S1c), which evidenced a uniform metal content, to support the fact that the expected product composition was attained by SHS, except for the minor oxide phases mentioned above.

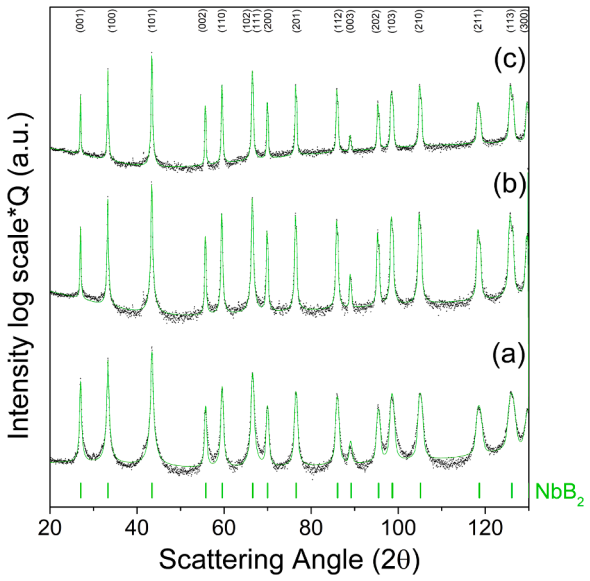

Fig. 1. XRD patterns and related Rietveld profiles of NB samples: (a) SHS powders, SPS products obtained at T_D= 1950 °C with (b) no graphite, and (c) after the addition of 1 wt% C. Experimental data (black dots) and NbB_2 refined phase (light green solid line) are reported. The light green Bragg's positions for NbB_2 are provided. The related structural parameters are reported in Supplementary Table S1.

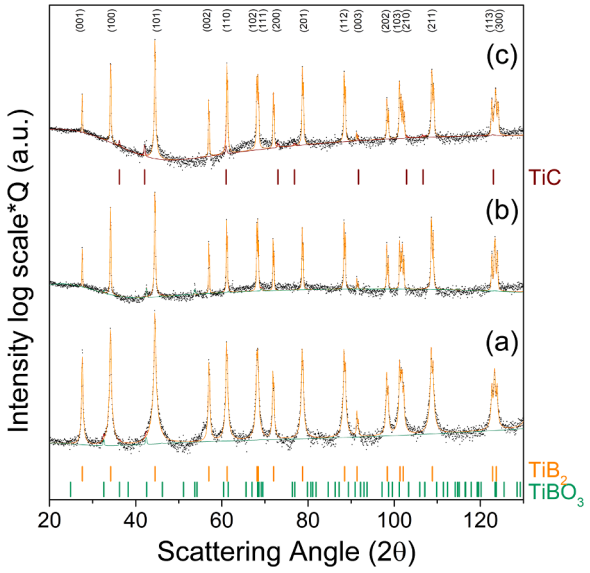

Fig. 2. XRD patterns and related Rietveld profiles of TB samples: (a) SHS powders, SPS products obtained at T_D= 1950 °C with (b) no graphite, and (c) after the addition of 1 wt% C. Experimental data (black dots), calculated intensity (red line), TiB_2 refined phase (orange solid line), $TiBO_3$ refined phase (green solid line) and TiC refined phase (brown solid line) are reported. Bragg's positions for all the phases are provided. The related structural parameters are reported in Supplementary Table S2.

Particle size parameters for these three sets of powders are reported in Table 1. Slightly coarser powders (d43 = 7.46μm) are obtained for the case of the HB system, while NB and TB showed more similar particle size, with d43 values of 4.86 and 3.24 μm, respectively.

Since the desired individual diboride phases were already obtained by SHS, there is no need to further transform residual reactants or

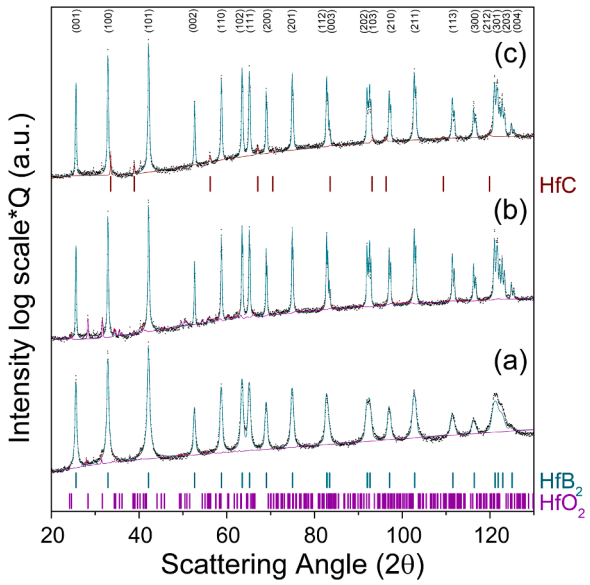

Fig. 3. XRD patterns and related Rietveld profiles of HB samples: (a) SHS powders, SPS products obtained at T_D= 1950 °C with (b) no graphite, and (c) after the addition of 1 wt% C. Experimental data (black dots), calculated intensity (red line), HfB_2 refined phase (dark cyan solid line), HfO_2 refined phase (purple solid line) and HfC refined phase (brown solid line) are reported. Bragg's positions for all the phases are provided. The related structural parameters are reported in Supplementary Table S3.

secondary products by SPS. Therefore, the different operating conditions adopted during the sintering step, which are summarized in Table 1, were aimed at maximizing the densification of the three batches of powders.

Let's consider first the case when no graphite was added to the SHS powders. As reported in Table 1, only the TB product reached a high densification level (98.2 %) after SPS at 1950 °C/20 min/20 MPa. In contrast, under the same conditions, NB and HB samples were scarcely consolidated, with relative densities equal to 90.7 and 88.3 %, respectively. The latter value is consistent with Musa et al. [35], who achieved densification levels of approximately 90 % when using the SHS-SPS method to obtain bulk HfB_2. On the other hand, the fabrication of NbB_2 utilizing this two-step route is investigated for the first time in this work.

As for their composition, no other phases, compared to the corresponding SHS powders, were detected by XRD analysis, whose results are reported in Figs. 1b-3b and supplementary Tables S1-S3. The presence of $TiBO_3$ and HfO_2 as secondary phases in TB and HB products, is therefore confirmed.

The Rietveld analysis also evidenced the crystallite size of NbB_2, TiB_2, and HfB_2 phases increased from 53, 88, and 52 nm to 120, > 200, and 155 nm, respectively, after SPS.

As shown in Figs. 4a, 4c, and 4e, the outcomes above are consistent with SEM/EDS observations. Indeed, the TB sample is highly consolidated (Fig. 4c), whereas NB and, above all, HB are not. Nonetheless, metals appear to be uniformly distributed into each ceramic. EDS analysis spectra performed in different regions, including pores, of the three samples are reported in supplementary Figures S2-S4. Even if no oxides were detected by XRD in the NB sample, EDS analysis evidenced the presence of some O-impurities inside pores (region (b) of Figure S2). The latter phase could be either amorphous or its amount is below the detection limit of XRD analysis. The low O-signals in both bulk and pore regions revealed by EDS for the case of TB (Figure S3), could be ascribed to the small amount of $TiBO_3$ identified by XRD analysis. Finally, no doubts regarding the presence of HfO_2 inside pores of HB specimens, as evidenced by EDS analysis results shown in Figure S4.

Table 1
Characteristics of SHS powders and related SPS products obtained in this work for the preparation of bulk single-phase NbB_2, TiB_2, HfB_2, $(Nb_{0.5}Ti_{0.5})B_2$, and $(Nb_{0.5}Hf_{0.5})B_2$ at different conditions.

System	SHS powders composition	SHS particle size parameters (μm)	SPS conditions T_D (°C)/t_D (min)/P (MPa)/xC (wt%)	Relative density ρ_r (%)
NB	Single phase	d10: 0.32 ± 0.10 d50: 2.29 ± 0.33 d90: 14.27 ± 1.53 d43: 4.86 ± 0.52	1850/20/20/0 1950/20/20/0 1950/20/20/1 2050/20/20/1	88.3 ± 0.6 90.7 ± 0.6 92.2 ± 1.0 92.4 ± 0.7
TB	Single phase	d10: 0.24 ± 0.09 d50: 1.42 ± 0.29 d90: 9.11 ± 0.93 d43: 3.24 ± 0.43	1950/20/20/0 1950/20/20/1	98.2 ± 0.3 98.9 ± 0.9
HB	Single phase	d10: 0.24 ± 0.04 d50: 1.84 ± 0.45 d90: 26.88 ± 4.88 d43: 7.46 ± 1.58	1950/20/20/0 1950/20/20/1	88.3 ± 0.1 97.2 ± 1.3
NHB	Multiple phases	d10: 0.40 ± 0.10 d50: 1.99 ± 0.31 d90: 17.36 ± 2.09 d43: 5.52 ± 0.71	2050/40/20/1	97.4 ± 0.2
NTB	Multiple phases	d10: 0.37 ± 0.12 d50: 2.02 ± 0.18 d90: 11.83 ± 0.86 d43: 4.12 ± 0.28	2050/20/20/1 2050/40/20/1	93.6 ± 0.8 93.5 ± 0.6

The oxides found on sintered samples, particularly for the case of HB, are thought to be the main responsible for the low densification level achieved during SPS. To remove them, graphite was added (1 wt%) to SHS powders prior to SPS, according to the beneficial effect observed when investigating other metal diboride systems on the base of the same strategy [7,8].

However, as reported in Table 1, the relative density of the NB sample was only slightly improved, from 90.7±0.6 to 92.2±1.0%, with the use of graphite. This outcome is also testified by the SEM micrograph shown in Fig. 4b. No detectable compositional differences were correspondingly evidenced by XRD analysis (Fig. 1c). Moreover, the attempt made to further reduce residual porosity by increasing the sintering temperature to 2050 °C only provided minor changes of NB sample density (92.4 ± 0.7 %).

Table 1 and Fig. 4d show that the already high densification achieved in the TB sample at 1950 °C with no additive (98.2 ± 0.3 %) was almost unaffected by the introduction of graphite (98.9 ± 0.9 %). Nonetheless, titanium borate was not detected anymore in the product, while a small amount of TiC (1.3 wt%) is correspondingly formed (Fig. 2c and supplementary Table S2).

$TiBO_3$ was also found as an intermediate product formed during the carbothermal synthesis of TiB_2 assisted by high-energy milling [36]. The transformation of $TiBO_3$ to TiB_2 was postulated to occur in the two following steps:

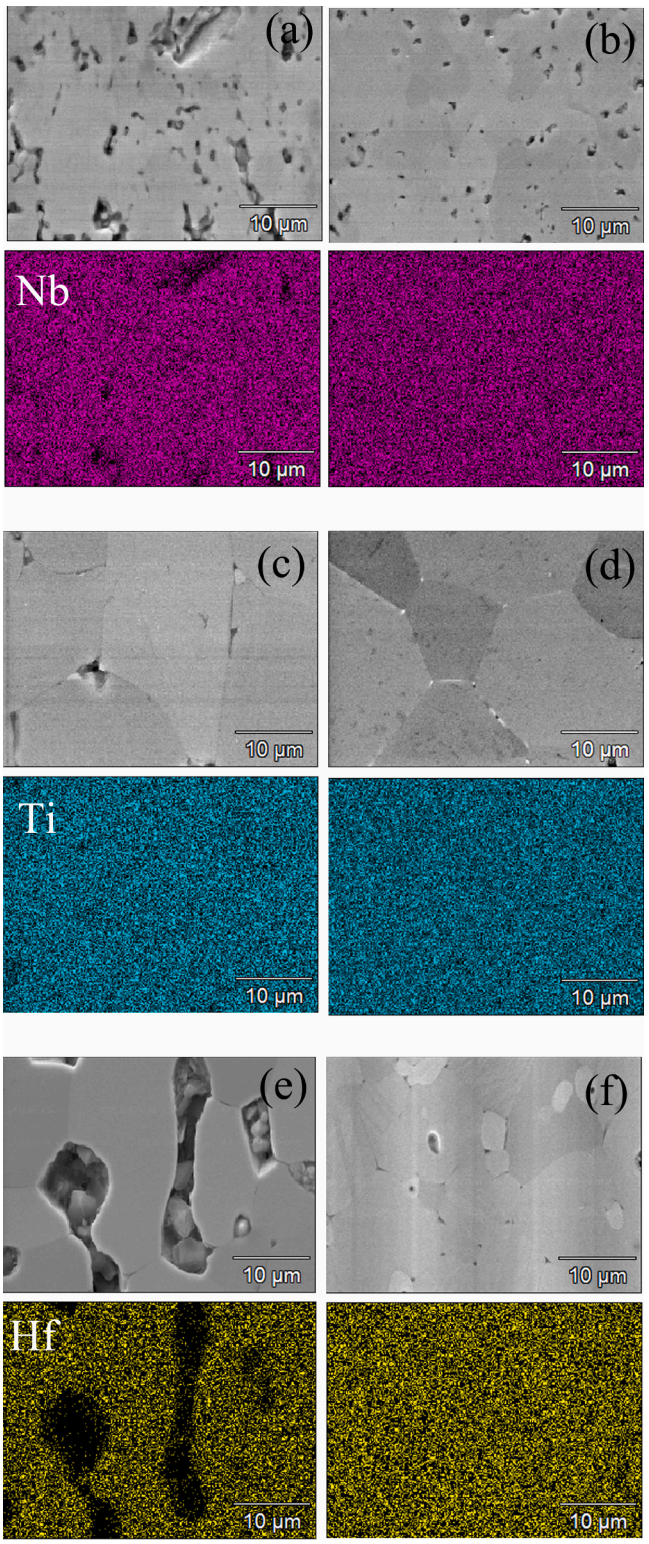

Fig. 4. SEM micrographs and associated EDS metal maps of individual diborides produced by SPS: NB obtained at 1950 °C/20 min/20 MPa with no graphite (a) and with 1 wt%C (b); TB prepared at 1950 °C/20 min/20 MPa with no graphite (c) and with 1 wt%C (d); HB produced at 1950 °C/20 min/20 MPa with no graphite (e) and with 1 wt%C (f).

$$TiBO_3 + 3\,C \rightarrow TiB + 3\,CO(g) \quad (1)$$

$$2TiB + B_2O_3 + 3C \rightarrow 2TiB_2 + 3CO(g) \quad (2)$$

which are likely to take place also in our study with the addition of graphite and the possible presence of B_2O_3 (in glassy form).

The major effect produced by graphite was observed when processing HB powders. Table 1 and Fig. 4f evidence the significant improvement obtained in sample density (from 88.3±0.1 to 97.2±1.3%). Furthermore, XRD analysis (Fig. 3c and supplementary Table S3) shows that HfO_2 was fully reduced by graphite and that HfC (3.1 wt%) was formed.

The small quantities of TiC and HfC detected in TB and HB products, respectively, affect only marginally the calculated values of relative densities, which remain roughly the same (TB) or slightly decrease, from 97.2 % to 97.1 % (HB), if these carbides are also considered. In addition, their presence is in line with similar results reported in the literature [4, 22], where secondary carbide phases were formed when graphitic carbon was used to remove O-contaminants in metal diborides. As explained elsewhere [7], the following reactions can be considered responsible for the carbothermal reduction of TiO_2 and HfO_2, as well as for the corresponding formation of TiC and HfC, respectively:

$$MO_2 + 2\,C \rightarrow M + 2CO \quad (3)$$

$$MO_2 + 3\,C \rightarrow MC + 2CO \quad (4)$$

where M=Ti or Hf.

Based on the results reported above, it is possible to state that the synthesis of the three individual diborides can be successfully obtained by SHS but only the resulting TiB_2 powders were highly densified by SPS at 1950 °C/20 min/20 MPa. The consolidation of the HB system was strongly promoted with the addition of 1 wt% of graphite, which was able to remove oxides contaminant originally present in SHS products. On the other hand, the introduction of such an additive determined only a modest improvement of the relative density of the NB ceramic. As evidenced by XRD analysis (cf. Fig. 1 and supplementary Table S1) and SEM/EDS results (Fig. 4), the latter system contained relatively lower amounts of oxide impurities, so that the major role played by graphite is to act as a solid lubricant rather than as a reducing agent [7,8], which apparently was not sufficient to achieve high consolidation levels. In any case, the obtained relative densities were adequate to provide samples for evaluating the oxidation and mechanical properties to be compared with those of the corresponding NHB and NTB ceramics.

3.2. Binary diborides

As for the cases of individual diborides, also the reaction fronts generated during the combustion synthesis of $(Nb_{0.5}Ti_{0.5})B_2$ and $(Nb_{0.5}Hf_{0.5})B_2$ from their elemental precursors were able to self-propagate across the related pellets. The measured average values of combustion wave velocity were both in the range 5–6 mm/s, i.e. in between to those obtained for the corresponding diboride constituents, as described in Section 3.1. Such values are also fairly consistent with those measured by Kurbatkina et al. [19] for $(Nb_{0.5}Hf_{0.5})B_2$, in the range of 3–7 mm/s.

However, differently from individual borides, the SHS process was unable to lead to the desired phases. For instance, when the NHB system was investigated, a multiphase product was obtained after SHS, with significant amounts of HfB_2 (27.6 wt%), and NbB_2 (18.7 wt%) also formed, along with the dominant $(Nb_{0.5}Hf_{0.5})B_2$ phase (53.1 wt%) (cf. Supplementary Figure S5 and supplementary Table S4). Traces of HfO_2 (0.6 wt%) were also detected. SEM/EDS observations further proved that Nb and Hf were not homogeneously distributed into the SHS powders (Figure S1d). Table 1 shows that particles' size after 1 h BM treatment (d43 = 5.52 μm) was in between to the values obtained for their individual counterparts.

Likewise, the SHS process did not succeed in fully converting initial precursors into $(Nb_{0.5}Ti_{0.5})B_2$. More specifically, according to the XRD analysis (Supplementary Figure S5 and supplementary Table S5), the resulting product contained, other than the equimolar phase (62.9 wt

%), also a NbB_2 (23.6 wt%), and a TiB_2 (13.5 wt%). The obtainment of a multiphase product reflects the inhomogeneous Nb and Ti distribution observed by SEM/EDS in SHS powders (Figure S1e). As for particle size (Table 1), slightly finer particles, compared to the NHB ones, were produced for the Ti-containing system (d43 = 4.12 μm), which is consistent with data obtained for the individual diborides.

Therefore, differently from the individual systems examined in Section 3.1, the role of the SPS stage for the fabrication of NHB and NTB ceramics must be considered twofold, i.e. not only aimed at consolidating SHS powders but also to transform secondary boride phases into the expected equimolar solid solutions. This was also the case of previous studies addressed to the preparation of binary [22,23] and quinary diborides [7,8], by SHS-SPS.

With the aim of identifying the milder sintering temperature and holding time conditions for achieving the latter goal, the effect produced when varying these two parameters on the resulting SPS products composition was systematically investigated.

The XRD patterns of samples obtained when processing NHB powders under different SPS conditions and in presence of graphite are shown in Fig. 5. The amount of each phase and the corresponding microstructural parameters evaluated by the Rietveld analysis are summarized in supplementary Table S4. These data evidence that an increase of either the sintering temperature from 1850 °C to 2050 °C (t_D=40 minutes) or the holding time from 20 to 40 minutes (T_D=2050 °C) determined a progressive improvement in the composition of the NHB product. On the other hand, secondary Nb-rich and Hf-rich $(Nb,Hf)B_2$ phases are detected in samples produced at T_D values lower than 2050 °C. This holds also true when operating at the latter temperature level but with t_D values shorter than 40 minutes. Therefore, the desired $(Nb_{0.5}Hf_{0.5})B_2$ phase with no secondary borides was achieved under the temperature/time conditions of 2050 °C/40 min.

As reported in Table 1, the resulting ceramic was 97.4 ± 0.2 % dense and also contained a low amount of $(Nb_{0.5}Hf_{0.5})C$ (2 wt%) (supplementary Table S4). Relative densities of all NHB samples, including those ones consisting of multiple phases after SPS, are summarized in supplementary Table S6.

The influence of the dwell temperature and the holding time on product composition was also examined for the case of the NTB system. Fig. 6 shows the XRD patterns of the sintered samples obtained with 1 wt %C when the dwell temperature increased from 1950 to 2050 °C (t_D=40 min) and the holding time was extended from 10 to 40 min (T_D=40 min). The corresponding phases content and microstructural parameters are listed in supplementary Table S5. The composition of the NTB product obtained after 40 min by SPS at 1950 °C with 1 wt%C was highly improved compared to that of SHS powders, but a relevant amount of a Nb-rich phase (8.7 wt%) was still found. Fig. 6 and supplementary Table S5 also reveal that the expected single-phase product was obtained as the dwell temperature increased to 2050 °C. Moreover, the study of the effect of the holding time at T_D= 2050 °C showed that an extension of this parameter from 10 to 20 minutes was sufficient to lead to the $(Nb_{0.5}Ti_{0.5})B_2$ solid solution with no secondary boride phases (Fig. 6 and supplementary Table S5).

The beneficial role played by graphite to promote the formation of the equimolar solid solutions in NHB and NTB systems is unequivocal. Indeed, when the additive-free SHS powders were directly exposed to the SPS conditions (2050 °C/40 min and 2050 °C/20 min for the NHB and NTB systems, respectively) that guarantee, with graphite, that the latter goal was achieved, a multiphase ceramic was produced (supplementary Figure S6 and related Tables S4 and S5). In particular, for the case of the NHB system, a Nb-rich phase (~20 wt%) was present

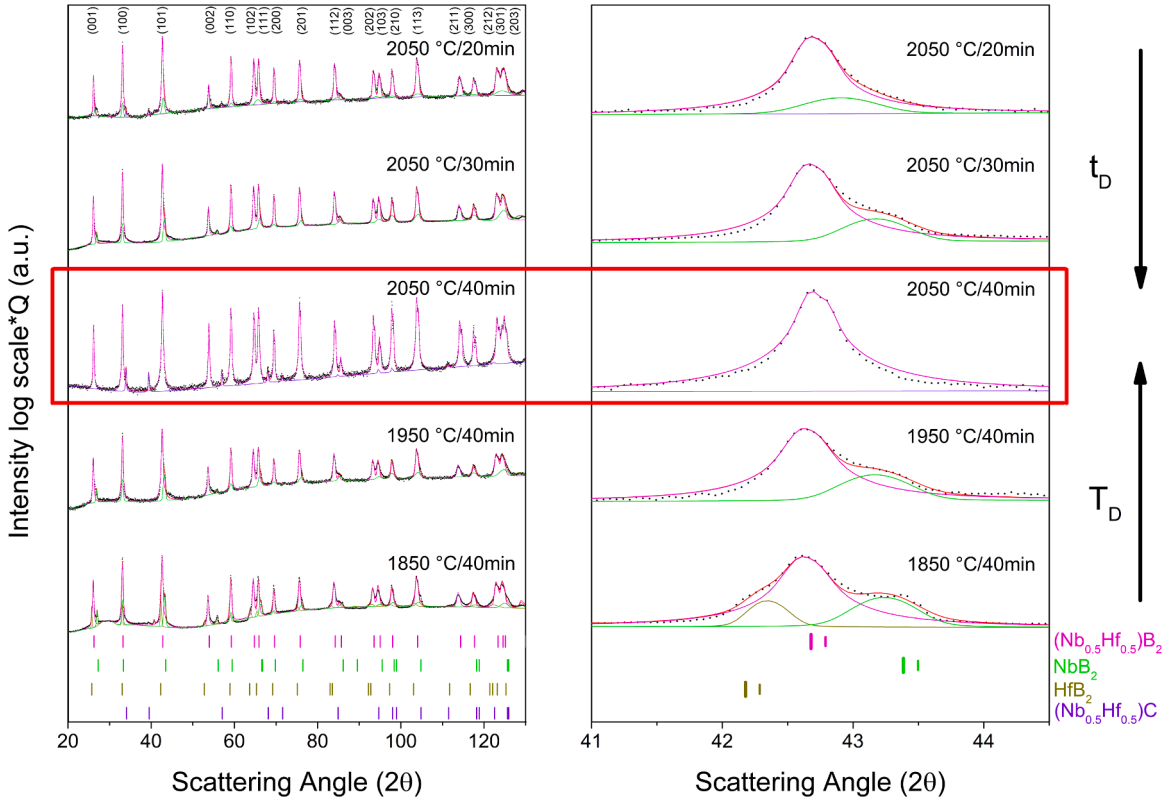

Fig. 5. XRD patterns and related Rietveld profiles of NHB samples produced by SPS, in presence of 1 wt% graphite, at different sintering temperatures and dwelling times. Experimental data (black dots), calculated intensity (red solid line), Hf-rich $(Nb,Hf)B_2$ refined phase which evolves into $(Nb_{0.5}Hf_{0.5})B_2$ in pattern 2050 °C/40 min (magenta solid line), Nb-rich $(Nb,Hf)B_2$ refined phase (light green solid line), HfB_2 refined phase (dark yellow solid line) and $(Nb_{0.5}Hf_{0.5})C$ refined phase (purple solid line) are reported. Bragg's positions for $(Nb_{0.5}Hf_{0.5})B_2$, NbB_2, HfB_2 and $(Nb_{0.5}Hf_{0.5})C$ phases are provided. Details on (101) reflections of metal diborides phases are reported on the right side. The related structural parameters are reported in Supplementary Table S4. The red frame includes the XRD pattern (general and detailed views) of the optimal NHB sample.

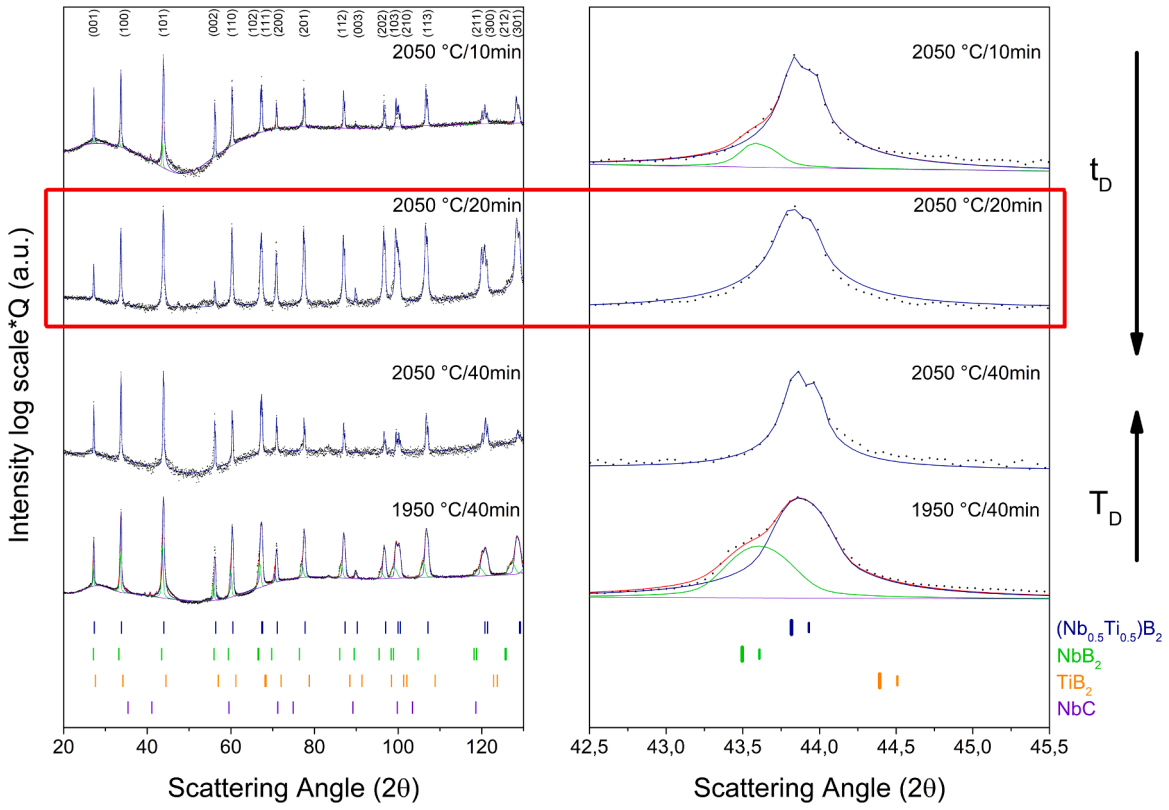

Fig. 6. XRD patterns and related Rietveld profiles of NTB samples produced by SPS, in presence of 1 wt% graphite, at different sintering temperatures and dwelling times. Experimental data (black dots), calculated intensity (red solid line), Ti-rich (Nb,Ti)B_2 refined phase which evolves into $(Nb_{0.5}Ti_{0.5})B_2$ in pattern 2050 °C/20 min and 2050 °C/40 min (blue solid line), Nb-rich (Nb,Hf)B_2 refined phase (light green solid line) and NbC refined phase (purple solid line) are reported. Bragg's positions for $(Nb_{0.5}Ti_{0.5})B_2$, NbB_2, TiB_2 and NbC phases are provided. Details on (101) reflections of metal diborides phases are reported on the right side. The related structural parameters are reported in Supplementary Table S5. The red frame includes the XRD pattern (general and detailed views) of the optimal NTB sample.

in the 89.7 % dense ceramic produced by SPS at 2050 °C/40 min (supplementary Table S4). Inhomogeneities and the presence of O-contaminants inside pores of graphite-free NHB sample are better proven in supplementary Figure S7, where the corresponding EDS analysis spectra are reported. SEM micrographs and related EDS maps shown in Figs. 7a-7b evidence that pores and Nb-richer zones (with no, or poorer in Hf) were nearly eliminated with the introduction of the reducing agent.

A Nb-rich phase (7.3 wt%) was also still found in the bulk NTB product obtained by SPS at 2050 °C/20 min with no graphite (supplementary Figures S8a-8b and related Table S5). Similarly to the case of the individual NB system, the use of such an additive provided only moderate benefits in terms of product consolidation, with an increase of the sample density from 92.8 ± 0.4 % (2050 °C, 0 wt%C) to 93.6 ± 0.8 % (2050 °C, 1 wt%C). As seen in Figs. 8a-8b, the results above, particularly product homogeneity, are confirmed by SEM/EDS outcomes. The SEM micrograph also shows that some large surface pores, and various cracks are present on the sample. This feature is expected to negatively affect mechanical properties, as discussed in Section 3.3.

It is worth mentioning that, when the fabrication by SHS-SPS of Nb-containing HEBs was carried out without using graphite as an additive [6], Niobium was one of the most difficult elements to solubilize into the ceramic matrix. Nb-rich zones were also observed by other authors in HEB ceramics fabricated using alternative processing methods [3,11,37]. Their presence was ascribed to the slow diffusion of Nb during the formation of the solid solution [11]. Thus, to promote the dissolution of this element, more severe sintering conditions were needed, which is also the case of binary diborides investigated in the present work. However, as discussed above, the use of graphite played also a favorable

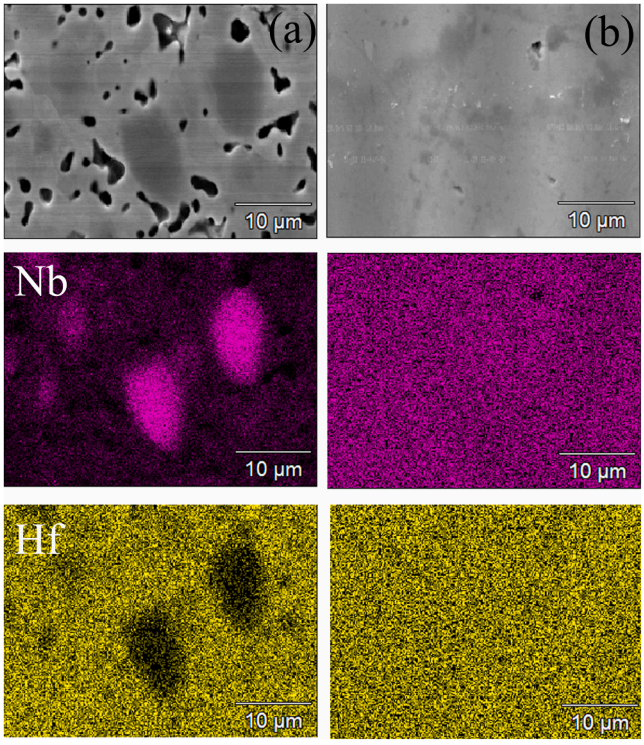

Fig. 7. SEM micrographs and associated EDS metal maps of NHB products obtained by SPS at 2050 °C/40 min/20 MPa: with no graphite (a) and with 1 wt %C (b).

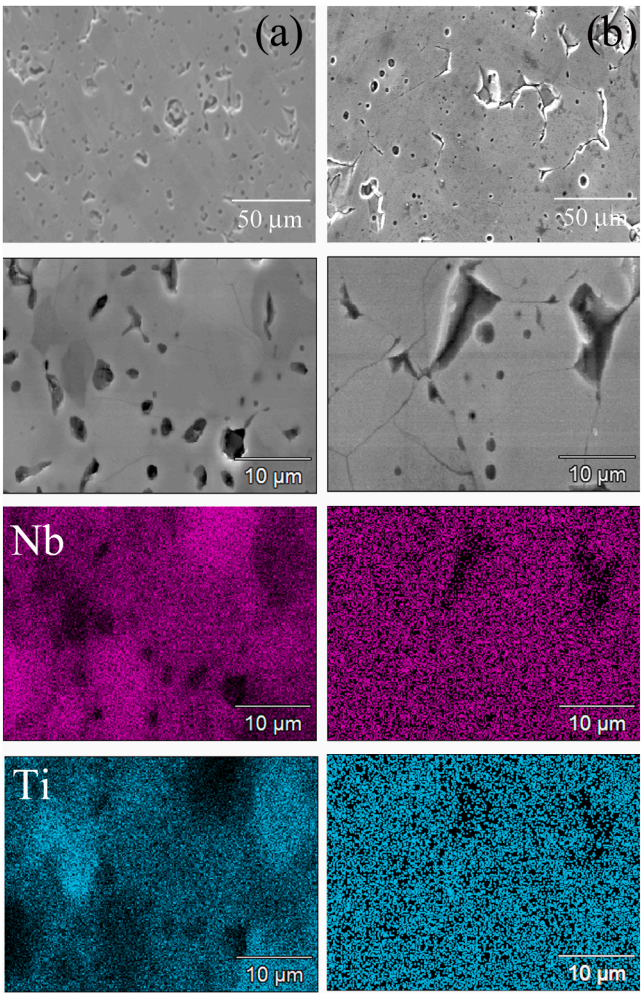

Fig. 8. SEM micrographs at different magnitudes and associated EDS metal maps of NTB products obtained by SPS at 2050 °C/20 min/20 MPa: with no graphite (a) and with 1 wt%C (b).

role in achieving this goal in the present study.

Grain size of diboride phases in NHB and NTB products varied from 5 to 30 μm, similarly to the individual boride samples, and in line with the values reported by Kurbatkina et al. [19] for the (Nb,Hb)B_2 solutions obtained in their work, in the range of 2–30 μm.

3.3. Mechanical properties

The measured Vickers hardness, Young's modulus and fracture toughness values of samples fabricated in this work under the SPS conditions which guaranteed the obtainment of the relatively denser and single-phase products are reported in Table 2.

Among the individual diborides, the TB sample displayed superior hardness (24.52 ± 1.99 GPa), while the HB sample exhibited the highest Young's modulus (581 ± 29 GPa). In contrast, the low densification level (92.2 ± 1.0 %) of the NB ceramic was detrimental for the corresponding mechanical properties. This is consistent with Maity et al. [14] findings, who measured Vickers hardness of 3.3 GPa for the 82.8 % dense NbB_2 sample they produced. On the other hand, values equal or above 20 GPa could be obtained for this system when reaching relative densities equal or exceeding 97 % [2,11,15]. The measured K_{IC} values of NB samples, for instance 4.01 ± 0.81 MPa $m^{1/2}$ when using the Evans and Charles formula (Table 2), are in line with literature data reported for the same system, in the range of 3.76–4 MPa $m^{1/2}$ [2,11,15]. TB and HB showed rather high elastic moduli, i.e. 548 ± 38 and 581 ± 29 GPa,

Table 2
Mechanical properties of bulk NB (ρ_r =92.2 ± 1.0 %), TB (ρ_r =98.9 ± 0.9 %), HB (ρ_r =97.2 ± 1.3 %), NTB (ρ_r =93.6 ± 0.8 %), and NHB (ρ_r =97.4 ± 0.2 %) samples produced by SPS in this work. EC: Evans and Charles; LF: Lawn and Fuller; EW: Evans and Wilshaw; L: Lankford; n.d.: not determined.

System	Hardness (GPa)	Young's Modulus (GPa)	K_{IC} (MPa $m^{1/2}$) Method
NB	15.47 ± 0.99	361 ± 21	4.01 ± 0.81 (EC), 2.51 ± 0.5 (LF), 3.71 ± 0.6 (EW), 6.8 ± 1.42 (L)
TB	24.52 ± 1.99	548 ± 38	3.28 ± 1.16 (EC), 2.05 ± 0.73 (LF), 3.01 ± 1.1 (EW), 4.49 ± 1.66 (L)
HB	17.38 ± 0.72	581 ± 29	3.87 ± 0.99 (EC), 2.42 ± 0.62 (LF), 3.58 ± 0.74 (EW), 7.09 ± 1.88 (L)
NTB	10.21 ± 2.01	324 ± 34	n.d.(*)
NHB	18.47 ± 0.60	586 ± 68	2.71 ± 1.06 (EC), 1.69 ± 0.67 (LF), 2.42 ± 1.12 (EW), 4.85 ± 1.98 (L)

(*) Multiple cracks formed on the samples' surface during indentation test.

respectively, which are similar to or even exceed the values obtained in previous investigations for such ceramics, in the range of 500–565 [2,30] and 445–480 GPa, respectively [2,38,39]. Nonetheless, higher hardness values were measured in the latter studies, up to 35 (TB) and 28 GPa (HB), respectively [2], whereas the K_{IC} values measured in the present work fall within the ranges of data reported in the literature for TiB_2 and HfB_2 [2,35,40].

Regarding the mechanical properties of binary diborides, the 97.4 % dense NHB ceramic exhibited Vickers hardness and Young's modulus equal 18.47 ± 0.60 GPa and 586 ± 68 GPa, respectively (Table 2). The latter values are very close, even slightly better, than those ones measured for the HB sample obtained in this work, 17.38 ± 0.72 GPa and 581 ± 29 GPa, respectively. A relatively lower elastic modulus (510 GPa) and a nanohardness (Berkovich tip) of 34.2 GPa were reported very recently by Kurbatkina et al. [19] for a 94 % dense $(Nb_{0.5}Hf_{0.5})B_2$ sample. No further studies are available in the literature on mechanical properties of $(Nb_{0.5}Hf_{0.5})B_2$.

Similarly to the case of NB, the modest powder consolidation (ρ_r =93.6 ± 0.8 %) achieved when processing NTB powders by SPS (2050 °C, 20 min, 20 MPa) can be considered responsible for the low values of Vickers hardness (10.21 ± 2.01 GPa) and Young's modulus (324 ± 34 GPa) correspondingly measured (Table 2). Moreover, for this sample, multiple cracks were generated on the samples' surface during indentation test, so that no reliable K_{IC} data could be obtained.

3.4. Oxidation resistance

Sintered NTB (2050 °C, 20 min, 1 %C) and NHB (2050 °C, 40 min, 1 %C) samples were exposed at high temperatures to flowing or stagnant air and their behavior was compared to those of the corresponding individual constituents also produced by SHS-SPS. Weight gain, compositional and structural changes occurring during oxidation tests, including the thickness of the formed oxide layer as well as its stability, were examined.

From the TGA curves reported in Fig. 9a, it is seen that the NTB sample (blue line) started to gain weight at about 800 °C, i.e. at a higher temperature compared to NB (green line, about 600 °C) and TB (orange line, about 700 °C) specimens. The relatively lower mass change of the binary specimen was kept up to about 1300 °C, above which the curve grew in an exponential manner.

Fig. 10a shows a different behavior for the NHB sample (magenta line), which began to gain mass at temperature slightly higher (approximately 650 °C) than that observed with the NB constituent

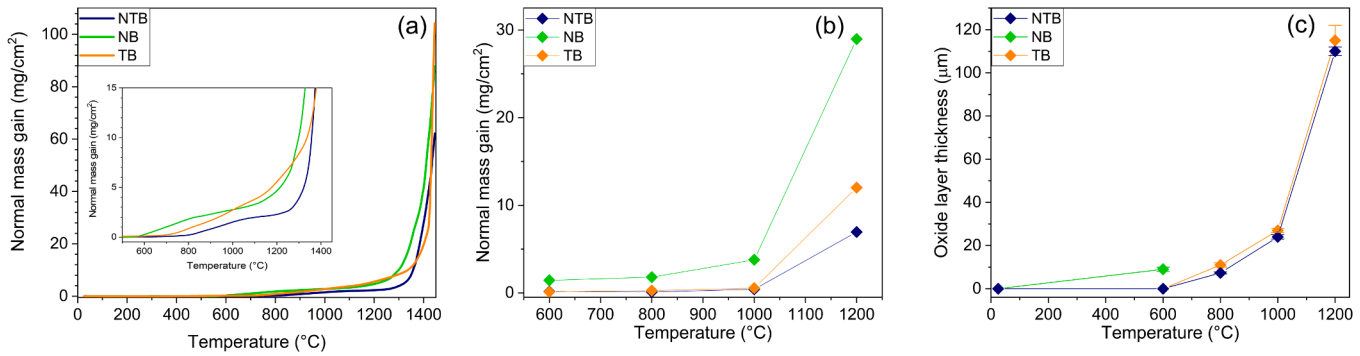

Fig. 9. Specific weight changes during (a) TGA oxidation test in air and (b) after 1 h in air furnace at 600, 800, 1000 and 1200 °C for the NTB, NB, TB samples produced in this work via SHS-SPS. (c) Oxide layer thickness of samples subjected to oxidation tests at different temperatures in air furnace. NB (green line and dots), TB (orange line and dots) and NTB (blue line and dots).

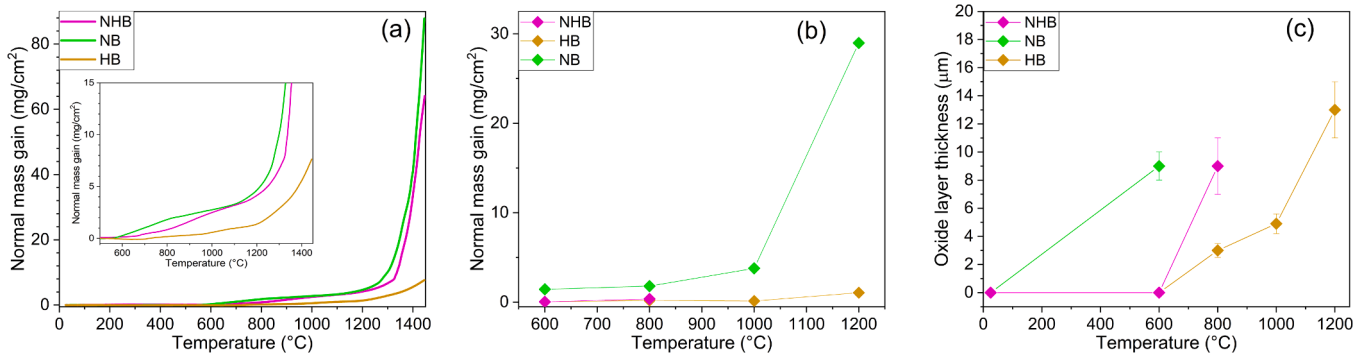

Fig. 10. Specific weight changes during (a) TGA oxidation test in air and (b) after 1 h in air furnace at 600, 800, 1000 and 1200 °C for the NHB, NB, HB samples produced in this work via SHS-SPS. (c) Oxide layer thickness of samples subjected to oxidation tests at different temperatures in air furnace. NB (green line and dots), HB (ochre line and dots) and NHB (magenta line and dots).

(green line), whereas a very little weight change took place in the HB ceramic (ochre line) for temperature below 1000 °C. Such performance was kept for the entire temperature range investigated, with the TGA curve of the binary system which follows, albeit staying slightly underneath, that of NB. In contrast, HB displayed much higher thermal stability, with a gradual and slower mass increase up to 1450 °C.

Outcome deriving from oxidation experiments in air furnace were consistent with TGA tests. Changes in samples appearance after the test conducted at different temperatures can be observed from the related optical images shown in supplementary Figures S9a-S9b. As for the individual systems, the oxide layer (white-yellow colored) formed on the NB ceramic processed at 800 °C separated from the sample, and this negative feature became progressively more relevant when more severe temperature conditions were applied. In contrast, no oxide scale exfoliation took place when heat treating TB samples, while their original gray-brown color turned to yellow-orange at 1000 °C, due to compositional transformations occurring on their surface, as discussed afterwards. Finally, HB samples were much less altered by the received treatment in air furnace.

Interestingly, the solid solution formed from the equimolar combination of NbB_2 and TiB_2 behaved like the latter diboride rather than the former one, with no detachment of the oxide layer (Figure S9b). In contrast, the presence of Niobium apparently played a prominent, negative, influence on the oxidation behavior of the NHB system, as demonstrated by the separation of the oxide scale from the bulk in samples exposed to 1000 °C or higher temperatures. In this regard, it should be considered that the NHB sample had a higher relative density compared to that of the NTB specimen, i.e. 97.4 and 93.6 %, respectively. Therefore, the oxidation behavior cannot be attributed to differences in samples' porosity since the less resistant sample also possessed higher relative density.

As shown in Fig. 9b, during tests in air furnace, NB samples increased their weight progressively up to 1000 °C, above which a significant mass gain is generated. The value of 28.9 mg/cm^2 measured at 1200 °C in the present work is reasonably in line with results obtained by Akin et al. [15], who reported, for the same temperature, an increase of mass gain from about 28 to approximately 50 mg/cm^2, as the exposure time was raised from 90 to 360 min, respectively. The marked rise in the NB weight as the temperature increased can be readily ascribed to the separation of the oxide layer (Figure S9a). Indeed, the latter cannot offer a protective barrier for the diffusion of oxygen, which can then reach more easily the sample bulk. On the other hand, lower changes were observed in TB and NTB products, the latter being apparently less affected by the oxidative environment, in accordance with the images depicted in Figures S9a-S9b.

As reported in Fig. 10b, a peculiar situation is encountered with the NHB system, which manifested, for temperatures exceeding 1000 °C, a lower rate in mass gain increase compared to that provided by TGA. Such discrepancies can be likely ascribed to the active role played by air flow during the latter test to enhance oxidation phenomena with respect to the case of furnace experiments conducted in stagnant air.

In what follows, the results above will be correlated with outcomes provided by XRD analysis performed on the surface of the annealed samples and SEM/EDS observations of the corresponding cross sections. Fig. 11(a) shows that Nb_2O_5 (orthorhombic) represents the major phase present on the surface of NB samples heat treated at 600 °C, with the original diboride phase still detected. This fact agrees with Ma et al. [41] who observed the onset of the oxidation of NbB_2 powders occurring at about 500 °C. The transformation of niobium pentoxide from the orthorhombic to monoclinic configuration occurred when the annealing

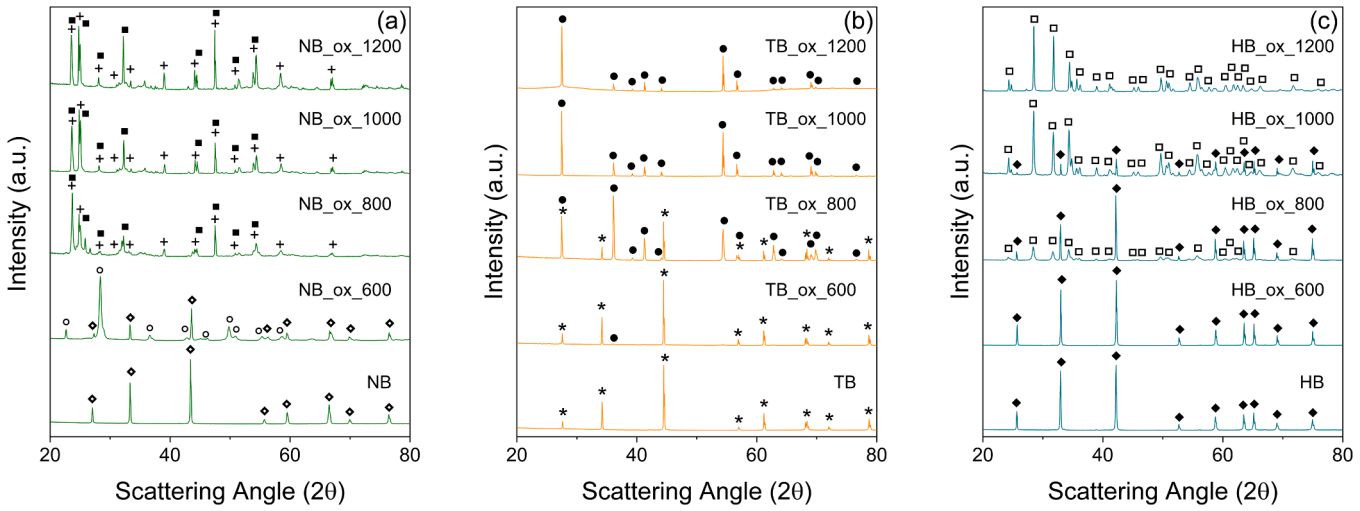

Fig. 11. XRD patterns relative to the surface of individual diborides samples after being heat treated in air furnace at different temperatures: NB (a), TB (b), HB (c). Patterns of NB_ox_800, NB_ox_1000, and NB_ox_1200 systems are related to the oxide layers separated during the test from the corresponding samples (cf. Fig. S9a). ⋄ NbB_2 hexagonal (COD-1510778), O Nb_2O_5 orthorhombic (PDF 30–10873), + Nb_2O_5 monoclinic (P 1 2/m 1) (COD 2107337 or PDF 27–1311), ■ Nb_3BO_9/ $3Nb_2O_5{\cdot}B_2O_3$ (PDF 19–0867), ★ TiB_2 hexagonal (COD-2002800), ● TiO_2 (rutile) tetragonal (PDF-21–1276), ◆ HfB_2 hexagonal (COD-1510711), □ HfO_2 monoclinic (COD-9013470).

temperature increased to 800 °C. This is consistent with Nico et al. [42], who reported that any Nb_2O_5 polymorph is transformed to m-Nb_2O_5 after a heat treatment in air. The only difference is that, in the present study, such a transformation was observed to occur at a lower temperature (800 °C) rather than for temperature exceeding 1000 °C [42]. Such discrepancy might be due to the systems undergoing oxidation being different, i.e. NbB_2 instead of elemental Niobium, respectively. In any case, the phase transition of NbO_2 from the orthorhombic to the monoclinic structure is accompanied by a marked cell volume expansion, from 706 to 1358 $(Å)^3$, respectively [42]. This feature could be then considered the main responsible for the separation of the oxide layer from the bulk occurred correspondingly (cf. Figure S9).

A niobium borate phase, ascribed to Nb_3BO_9 ($3\,Nb_2O_5{\cdot}B_2O_3$), was also formed at 800 °C during the oxidation of NB sample. Its presence was also observed by Akin et al. [15] who postulated the occurrence of the following reaction:

$$3Nb_2O_5\ (s) + B_2O_3\ (l) \rightarrow 2Nb_3BO_9\ (s) \quad (5)$$

According to XRD analysis, the relative content of niobium borate progressively increases as the temperature was raised up to 1200 °C.

The heat treatment at 600 °C of the TB sample resulted in the incipient formation of TiO_2 (Fig. 11b), which is congruent with the fact

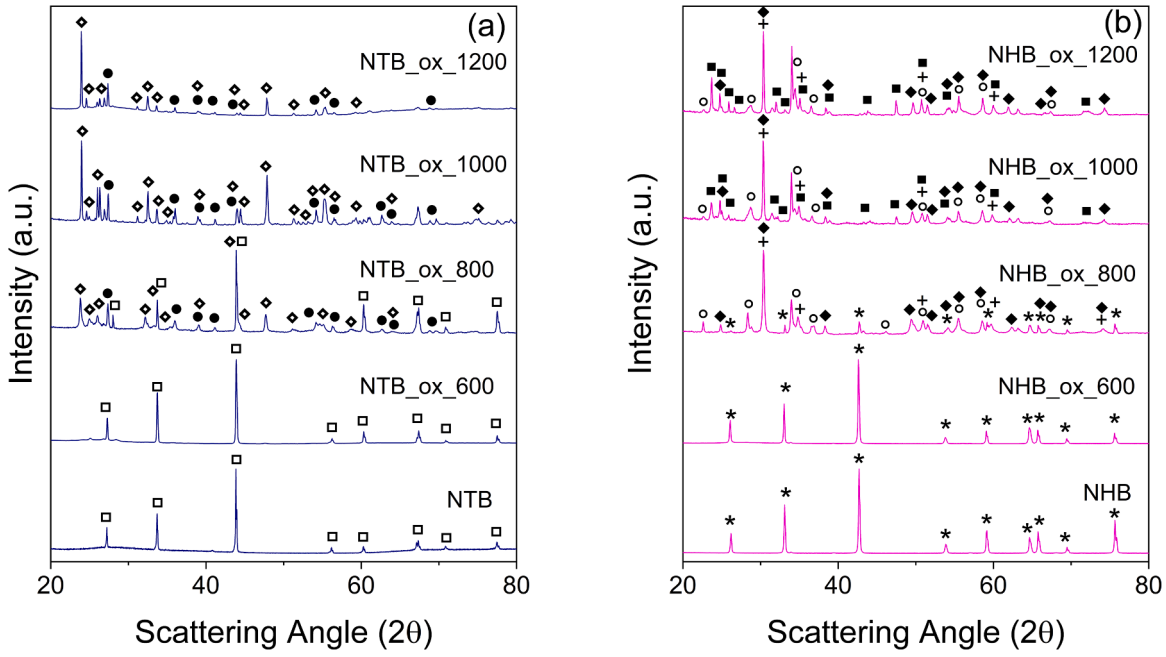

Fig. 12. XRD patterns relative to the surface of binary diborides samples after being heat treated in air furnace at different temperatures: NTB (a), and NHB (b). Patterns of NHB_ox_1000, and NHB_ox_1200 systems are related to the oxide layers separated during the test from the corresponding samples (cf. Figs. S9a and S9b). □ $(Nb_{0.5}Ti_{0.5})B_2$ hexagonal (COD-1510775), ● $TiB_{0.024}O_2$ tetragonal (PDF-87–0921), ⋄ $TiNb_2O_7$ monoclinic (PDF-39–1407), ★ $(Hf_{0.5}Nb_{0.5})B_2$ hexagonal (COD-1510708), O Nb_2O_5 monoclinic (Pearson 1232958), + HfO_2 cubic (PDF-53–0560), ◆ $Nb_{16.8}O_{42}$ orthorhombic (COD 2106534), ■ $Nb_{12}O_{29}$ orthorhombic (COD (1541318).

that the beginning of TiB_2 oxidation in air occurs in the range 400–500 °C [40]. XRD peaks intensity of the latter phase becomes notably higher in samples exposed at 800 °C, with lower amounts of TiB_2 still found. Finally, when the test was conducted at higher temperatures (1000 or 1200 °C), TiO_2 was the only phase evidenced by this analysis.

XRD patterns shown in Fig. 11c indicate that no oxidation occurred on HB samples annealed at 600 °C. In addition, while HfO_2 was detected on samples processed at 800 °C, HfB_2 still represented the dominant phase. As the temperature was further increased, the latter one was progressively replaced by HfO_2, which was the only phase found in samples heat treated at 1200 °C.

The substitution of 50 at% Nb with Ti apparently provided a delay in the oxidation of the diboride phase. Indeed, in contrast with the NB system, no oxides were detected by XRD analysis on the surface of the NTB sample at 600 °C (Fig. 12a). However, a mixed oxide and a B-poor titanium borate, associated to $TiNb_2O_7$ and $TiB_{0.024}O_2$, respectively, were found at 800 °C, along with the original $(Nb_{0.5}Ti_{0.5})B_2$ phase. The latter one completely disappeared at temperatures equal to or exceeding 1000 °C. Based on XRD analysis (Fig. 12a), and in agreement with the TiO_2-Nb_2O_5 phase diagram [43,44], $TiNb_2O_7$, once formed, did not undergo any structural transformation as temperature was raised to 1200 °C. Moreover, no Nb_2O_5 was detected, differently from the case of individual NB sample, where volume changes associated to its orthorhombic to monoclinic phase transition were considered responsible for the observed detrimental oxidation behaviour. Consequently, the formation of the more stable mixed oxide made the oxide layer generated on NTB ceramics relatively less stressed, i.e. less prone to exfoliate, differently from that formed on the NB sample, where the o- to m-Nb_2O_5 phase transition took place (Figure S9).

Consistently with the higher thermal stability of HfB_2 in air (Fig. 11c), the replacement of 50 at% Nb with Hf also produced beneficial effects, at least at low temperatures, as testified by the absence of oxides in the XRD pattern of NHB sample annealed at 600 °C (Fig. 12b). Nonetheless, an increase of the temperature to 800 °C was accompanied by remarkable compositional changes, with the ceramic surface mainly consisting of two niobium oxides, i.e. Nb_2O_5 (monoclinic) and $Nb_{16.8}O_{42}$ (orthorhombic), along with HfO_2. A residual amount of $(Hf_{0.5}Nb_{0.5})B_2$ was also found. As the temperature in the furnace was raised to 1000 °C, the original diboride was not detected on the sample surface, and the formed oxide layer separated (Figure S9b), whereas a new niobium oxide, associated to $Nb_{12}O_{29}$ (orthorhombic), was detected together with Nb_2O_5, $Nb_{16.8}O_{42}$, and HfO_2. No further compositional changes were observed at 1200 °C. The cell volume of o-$Nb_{12}O_{29}$ (303 $(Å)^3$) formed at 1000 °C is significantly smaller than those of m-Nb_2O_5 (1358 $(Å)^3$) and o-$Nb_{16.8}O_{42}$ (708 $(Å)^3$ [42], already present at 800 °C. Therefore, as for the case of the NB system described previously, the oxide detachment in the NHB sample at 1000 °C observed in Figure S9 can be attributed to the corresponding volume changes accompanying such phase transformation. Although the formation of mixed oxides in the Nb-Hf-O system is possible [45], their presence was not detected in our experiments, differently to the case of the NTB sample, where the stable $TiNb_2O_7$ phase was produced.

SEM/EDS investigations evidenced the formation of an oxide layer on the surface of each diboride ceramic. As reported in Figs. 9c and 10c, the thickness of such layers monotonically increased as the oxidation temperature was augmented. In particular, the oxide covering the NB ceramic heat treated at 600 °C, above which it separated from the rest of the sample (Figure S9a), was 9 ± 1 μm thick whereas, consistently with XRD findings, SEM/EDS observations confirm TB and NTB samples were not, or only barely, affected by the oxidizing environment at 600 °C. At 800 °C or higher values, an oxide layer with a growing and comparable thickness was formed on the latter two ceramics. For instance, the layers produced at 1200 °C on TB and NTB samples were 115 ± 7 and 110 ± 2 μm thick, respectively. Based on the outcomes described above, the less resistant system during oxidation experiments was undoubtedly NB followed by TB, while their equimolar combination produced a solid solution with relatively higher stability compared to its constituents.

Fig. 10c shows that the thickness of the oxide layer formed on the Hf-containing binary sample (magenta line and dots) is in between to those of its individual constituents (green and ochre lines-dots for NB and HB, respectively). Due to the separation of the oxide formed on NB and NHB samples for temperatures equal to or above 800 and 1000 °C, a complete comparison of these data is not possible in the whole temperature range. Nonetheless, these data and the corresponding mass gain measured after the same test (Fig. 10b) allow us to state that the three systems exhibited higher sensitivity to the oxidizing environment in the following order: NB>NHB>HB.

The cross sections of samples relative to the temperature conditions above which the separation of the oxide layers occurred were examined in more detail by SEM/EDS, as shown in Fig. 13. Local EDS analysis spectra performed on the bulk side and on the oxide layer of the various samples are also reported in supplementary Figure S10.

It is seen that the exposition of the NB ceramic to air at 600 °C determined a significant sample degradation. In particular, the generated oxide layer was very porous and friable, so that it was significantly removed during polishing. This is the reason why EDS signals on this layer are very weak (cf. Figure S10) and the O-map irrelevant (not reported in Fig. 13). Fig. 13 also evidences that the 115 ± 7 μm thick oxide product formed at 1200 °C on the TB sample is apparently well attached to the bulk, but it is also very irregular and porous. In contrast, under the same annealing condition, a very thin (13 ± 2 μm) and compact layer of HfO_2 is produced on the surface of the HB ceramic. This finding confirms the superior oxidation resistance of HfB_2, as a consequence of the fact that the volume contraction accompanying phase transition of the formed HfO_2 from the monoclinic to tetragonal structure, and the consequent formation of cracks and other defects, takes place at high temperatures, near to 1800 °C [17], i.e. well above of the conditions adopted in this work.

Let's consider now the behavior of the two-components ceramics. The oxide layer formed at 1200 °C on the NTB sample displays an irregular microstructure while it is more compacted compared to that generated at the same condition on the TB ceramics. This finding is coherent with the relatively lower mass gain exhibited at 1200 °C by the first system with respect to the second one, as shown in Fig. 9b. It is then confirmed that the solid solution resulting when coupling Nb and Ti diborides in equimolar proportion is thermally more resistant compared to the individual constituents.

As for the NHB product heat treated at 800 °C, a beneficial effect was provided by the replacement of 50 at% Nb with Hf, which allowed the oxide layer to resist at higher temperatures (200 °C above) with respect to that formed on the NbB_2 sample. Nonetheless, such benefit ceased as the temperature was raised to 1000 °C, under which the oxide layer separation occurred (Figure S9b). As discussed previously, the latter event corresponded to the phase transformations involving niobium oxides formed in both NB and NHB samples as the oxidation temperature was progressively raised. These compositional changes are accompanied by volume expansion/contraction phenomena and, consequently, thermomechanical stresses are generated in the oxide scales, which make them less stable and prone to detach from the sample, as experimentally observed. The latter statement is supported by the fact that such an event was not observed when heat treating TB, HB, and NTB ceramics (Figures S9a-S9b), since the related oxides did not undergo any phase transition as the temperature increased from 600 to 1200 °C (Figs. 11b, 11c, 12a).

4. Concluding remarks

Equimolar $(Nb,Ti)B_2$ and $(Nb,Hf)B_2$ solid solutions are successfully produced in this work by the SHS-SPS method starting from elemental powders and using graphite as additive. Differently from the case of individual diboride constituents, SHS was unable to lead to single phase

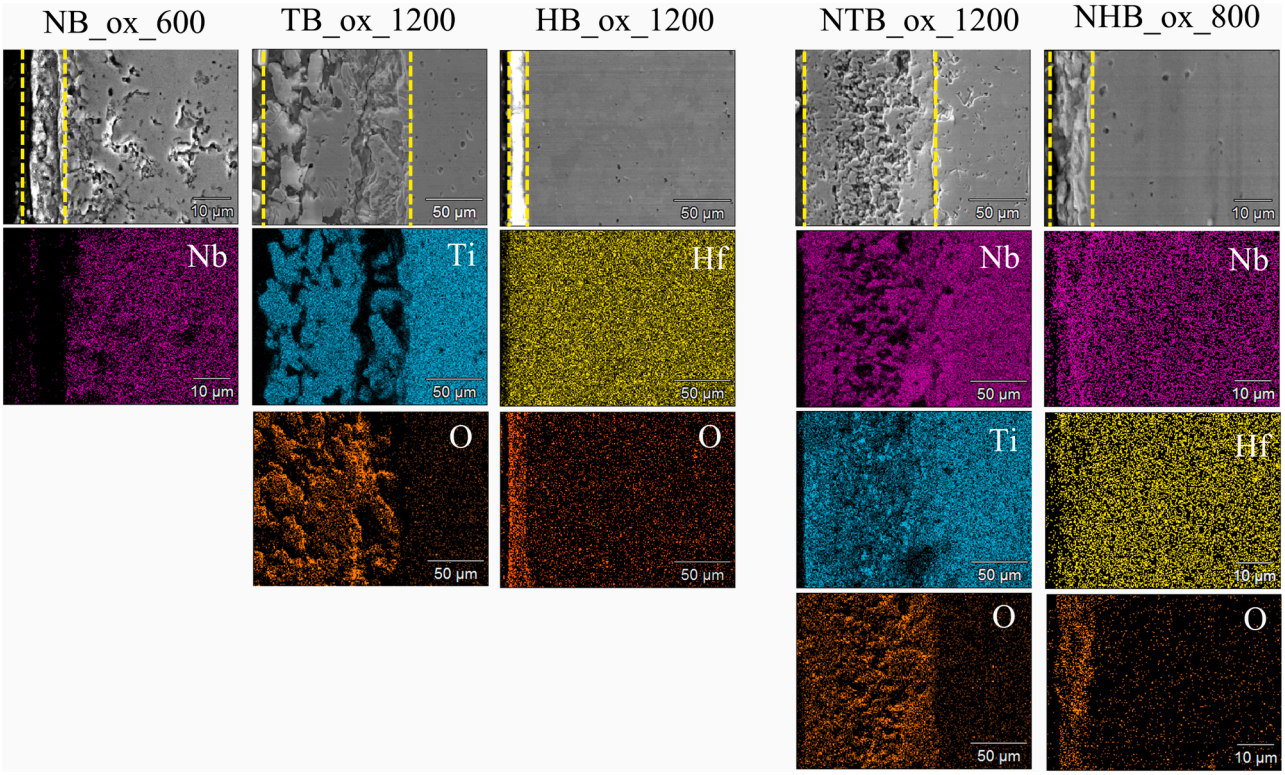

Fig. 13. Cross sectional SEM micrographs and corresponding EDS elemental maps of samples after receiving 1 h heat treament in air furnace under the highest temperature condition where no separation of the formed oxide layer was observed: NB (600 °C), TB (1200 °C), HB (1200 °C), NTB (1200 °C), and NHB (800 °C). The corresponding EDS spectra carried out on the bulk side and the oxide layer are reported in supplementary Fig. S10.

binary diborides. The latter goal was reached after processing the two SHS powders by SPS at 2050 °C/20 MPa, while a longer holding time was requested by NHB (40 min) as compared to NTB (20 min). Graphite played a relevant role to promote, during SPS, the conversion of secondary phases found in SHS powders into the desired equimolar diborides. NHB powders consolidation was also highly facilitated by the introduction of such an additive, with an increase of the relative density from 89.7 % to 97.4 %. On the other hand, a modest effect (relative density from 92.8 % to 93.6 %) was observed when considering the NTB sample. This fact was consistent with the behaviour displayed by individual diborides and it could be ascribed to the major beneficial effect produced by graphite to reduce oxide contaminants in Hf containing systems.

Measured Vickers hardness (18.47 GPa) and Young's modulus (586 GPa) of $(Nb_{0.5}Hf_{0.5})B_2$ were slightly better than those ones of the HfB_2 ceramic, i.e. 17.38 GPa and 581 GPa, respectively. In contrast, the mechanical properties of NTB sample were negatively affected, similarly to the NbB_2 product, by its inadequate densification level.

The oxidation behaviour of $(Nb_{0.5}Hf_{0.5})B_2$ was in between to those manifested by HfB_2 and NbB_2 product. Interestingly, a relatively lower mass gain, accompanied by a smaller oxide scale thickness, compared to its constituents, was observed after oxidation tests of $(Nb_{0.5}Ti_{0.5})B_2$ specimens. On the other hand, NB and NHB appeared to be the most sensitive systems to the oxidation environment, with the formed oxide layers which separate from the bulk when the two samples were exposed to 600 and 800 °C, respectively. Such feature can be associated to the compositional changes occurring in the oxide layer formed on the samples surface. In particular, during oxidation of NbB_2, the phase transition from o- to m-Nb_2O_5 took place at 800 °C. Analogously, the o-$Nb_{12}O_{29}$ phase was formed at 1000 °C, in addition to m-Nb_2O_5 and $Nb_{16.8}O_{42}$ already present in the $(Nb_{0.5}Hf_{0.5})B_2$ sample heat treated at 800 °C. Such chemical transformations are accompanied by significant volume contraction/expansions, and the resulting thermomechanical stresses in the oxide layers provoke their separation from the samples. Conversely, more stable oxide scales were generated on the surface of TB, HB, and NTB ceramics, where the types of oxide did not change in the whole temperature range investigated (600–1200 °C). In particular, the formation of a mixed oxide ($TiNb_2O_7$), which did not undergo any phase transition, during the oxidation of the NTB sample was highly beneficial to generate a more stable oxide scale.

More detailed studies, including quantitative XRD analysis, required to evaluate the amount of each oxide phase formed at increasing temperatures, thus clarifying the extent to which the transforming phases contribute to volume changes, will be provided in future works. Possible improvements on the characteristics of these ceramics, will be also investigated soon. For instance, following Feng et al. [11] work, the effect deriving by the presence of a Nb-rich secondary solid solution for the suppression of grain growth and the concurrent improvement of Vickers hardness and Young's modulus is worth to be examined.

CRediT authorship contribution statement

Cappai Luca: Writing – review & editing, Methodology, Investigation, Data curation. **Casu Mariano:** Writing – review & editing, Methodology, Investigation, Data curation. **Locci Antonio M:** Writing – review & editing, Validation, Supervision, Conceptualization. **Cao Giacomo:** Writing – review & editing, Resources, Funding acquisition, Conceptualization. **Garroni Sebastiano:** Writing – review & editing, Validation, Methodology, Formal analysis, Data curation. **Bellucci Devis:** Writing – review & editing, Validation, Methodology, Investigation, Data curation. **Cannillo Valeria:** Writing – review & editing, Validation, Methodology, Investigation, Data curation. **Orru' Roberto:** Writing – review & editing, Writing – original draft, Validation, Supervision, Resources, Funding acquisition, Data curation, Conceptualization.

Declaration of Competing Interest

The authors declare the following financial interests/personal relationships which may be considered as potential competing interests: Roberto Orru' reports financial support was provided by Italian Ministry for Research and Education (MUR). Giacomo Cao reports financial support was provided by Italian Ministry for Research and Education (MUR). If there are other authors, they declare that they have no known competing financial interests or personal relationships that could have appeared to influence the work reported in this paper.

Acknowledgements

One of the authors (Mariano Casu) performed his activity in the framework of the Ph.D. in Innovation Sciences and Technologies at the University of Cagliari, Italy. We acknowledge financial support under the National Recovery and Resilience Plan (NRRP), Mission 4, Component 2, Investment 1.1, Call for tender No. 104 published on 2.2.2022 by the Italian Ministry of University and Research (MUR), funded by the European Union—NextGenerationEU—Project Title I-CREATE—Innovative Class of REfrActory ceramics for extreme Environments—CUP F53D23002020006—Grant Assignment Decree No. 104 adopted on 2 February 2022 by the Italian Ministry of Ministry of University and Research (MUR). The financial contribution by Italian Ministry for Research and Education (MUR) under the National Recovery and Resilience Plan (NRRP)—Mission 4, Component 2, "From research to business" INVESTMENT 1.5, "Creation and strengthening of Ecosystems of innovation" and construction of "Territorial R&D Leaders", project eINS—Ecosystem of Innovation for Next Generation Sardinia (cod. ECS 00000038) is also acknowledged.

The authors acknowledge the GAUSS-CeSAR (Centro Servizi d'Ateneo per la Ricerca) of the Universities of Cagliari (Italy) and Sassari (Italy) for X-ray diffraction analyses.

Appendix A. Supporting information

Supplementary data associated with this article can be found in the online version at doi:10.1016/j.jeurceramsoc.2025.117277.

References

[1] W.G. Fahrenholtz, G.E. Hilmas, Ultra-high temperature ceramics: materials for extreme environments, Scr. Mater. 129 (2017) 94–99, https://doi.org/10.1016/j.scriptamat.2016.10.018.

[2] B.R. Golla, A. Mukhopadhyay, B. Basu, S.K. Thimmappa, Review on ultra-high temperature boride ceramics, Prog. Mater. Sci. 111 (2020) 100651, https://doi.org/10.1016/j.pmatsci.2020.100651.

[3] Gild, Y. Zhang, T. Harrington, S. Jiang, T. Hu, M.C. Quinn, W.M. Mellor, N. Zhou, K. Vecchio, J. Luo, High-entropy metal diborides: a new class of high-entropy materials and a new type of ultrahigh temperature ceramics, Sci. Rep. 6 (2016) 37946, https://doi.org/10.1038/srep37946.

[4] J. Gild, K. Kaufmann, K. Vecchio, J. Luo, Reactive flash spark plasma sintering of high-entropy ultrahigh temperature ceramics, Scr. Mater. 170 (2019) 106–110, https://doi.org/10.1016/j.scriptamat.2019.05.039.

[5] Y. Zhang, W.-M. Guo, Z.-B. Jiang, Q.-Q. Zhu, S.-K. Sun, Y. You, K. Plucknett, H.-T. Lin, Dense high-entropy boride ceramics with ultra-high hardness, Scr. Mater. 164 (2019) 135–139, https://doi.org/10.1016/j.scriptamat.2019.01.021.

[6] G. Tallarita, R. Licheri, S. Garroni, S. Barbarossa, R. Orrù, G. Cao, High-entropy transition metal diborides by reactive and non-reactive spark plasma sintering: a comparative investigation, J. Eur. Ceram. Soc. 40 (4) (2020) 942–952, https://doi.org/10.1016/j.jeurceramsoc.2019.10.031.

[7] S. Barbarossa, R. Orrù, S. Garroni, R. Licheri, G. Cao, Ultra high temperature high-entropy borides: effect of graphite addition on oxides removal and densification behaviour, Ceram. Int. 47 (5) (2021) 6220–6231, https://doi.org/10.1016/j.ceramint.2020.10.200.

[8] S. Barbarossa, R. Orrù, V. Cannillo, A. Iacomini, S. Garroni, M. Murgia, G. Cao, Fabrication and characterization of quinary high entropy-ultra-high temperature diborides, Ceramics 4 (2) (2021) 108–120, https://doi.org/10.3390/ceramics4020010.

[9] M. Gaboardi, F. Monteverde, F. Saraga, G. Aquilanti, L. Feng, W. Fahrenholtz, G. Hilmas, Local structure in high-entropy transition metal diborides, Acta Mater. 239 (2022) 118294, https://doi.org/10.1016/j.actamat.2022.118294.

[10] L. Feng, W.G. Fahrenholtz, D.W. Brenner, High-entropy ultra-high-temperature borides and carbides: a new class of materials for extreme environments, Annu. Rev. Mater. Res. 51 (2021) 165–185, https://doi.org/10.1146/annurev-matsci-080819-121217.

[11] L. Feng, W.G. Fahrenholtz, G.E. Hilmas, F. Monteverde, Effect of Nb content on the phase composition, densification, microstructure, and mechanical properties of high-entropy boride ceramics, J. Eur. Ceram. Soc. 41 (1) (2021) 92–100, https://doi.org/10.1016/j.jeurceramsoc.2020.08.058.

[12] K. Sairam, J.K. Sonber, T.S.R.Ch Murthy, C. Subramanian, R.K. Fotedar, R.C. Hubli, Reaction spark plasma sintering of niobium diboride, Int. J. Refract. Met. Hard Mater. 43 (2014) 259–262, https://doi.org/10.1016/j.ijrmhm.2013.12.011.

[13] D. Demirskyi, I. Solodkyi, T. Nishimura, Y. Sakka, O. Vasylkiv, High-temperature strength and plastic deformation behavior of niobium diboride consolidated by spark plasma sintering, J. Am. Ceram. Soc. 100 (11) (2017) 5295–5305, https://doi.org/10.1111/jace.15048.

[14] T.N. Maity, K. Biswas, B. Basu, Critical role of ZrO_2 on densification and microstructure development in spark plasma sintered NbB_2, Acta Mater. 152 (2018) 215–228, https://doi.org/10.1016/j.actamat.2018.03.049.

[15] I. Akin, B.C. Ocak, F. Sahin, G. Goller, Effects of SiC and SiC-GNP additions on the mechanical properties and oxidation behavior of NbB_2, J. Asian Ceram. Soc. 7 (2) (2019) 170–182, https://doi.org/10.1080/21870764.2019.1595929.

[16] D.S. Arati, S.R.C. Murthy Tammana, J.K. Sonber, B. Paul, S. Majumdar, A.K. Tyagi, Studies on synthesis and densification of niobium diboride using carbothermic reduction and hot pressing, Int. J. Refract. Met. Hard Mater. 112 (2023) 106119, https://doi.org/10.1016/j.ijrmhm.2023.106119.

[17] J.E. Förster, W.G. Fahrenholtz, G.E. Hilmas, G.E. Naraparaju, R. Oxidation behavior of Nb-coated zirconium diboride, J. Eur. Ceram. Soc. 43 (12) (2023) 5174–5182, https://doi.org/10.1016/j.jeurceramsoc.2023.04.029.

[18] T. Wen, B. Ye, H. Liu, S. Ning, C.-Z. Wang, Y. Chu, Formation criterion for binary metal diboride solid solutions established through combinatorial methods, J. Am. Ceram. Soc. 103 (5) (2020) 3338–3348, https://doi.org/10.1111/jace.16983.

[19] V.V. Kurbatkina, E.I. Patsera, T.A. Sviridova, N.A. Kochetov, E.A. Levashov, Combustion synthesis and characterization of ultra-high-temperature NbB_2–HfB_2 solid solutions, Int. J. Self Propagating High Temp. Synth. 32 (4) (2023) 313–325, https://doi.org/10.3103/S1061386223040143.

[20] D. Demirskyi, I. Solodkyi, T. Nishimura, O.O. Vasylkiv, Fracture and property relationships in the double diboride ceramic composites by spark plasma sintering of TiB_2 and NbB_2, J. Am. Ceram. Soc. 102 (7) (2019) 4259–4271, https://doi.org/10.1111/jace.16276.

[21] M. Kaplan Akarsu, I. Akin, Production and characterization of spark plasma sintered $(Ti,Nb)B_2$ solid solutions with graphene nanoplatelets and hexagonal boron nitride, Ceram. Int. 49 (4) (2023) 5582–5594, https://doi.org/10.1016/j.ceramint.2022.10.155.

[22] S. Barbarossa, M. Casu, R. Orrù, A.M. Locci, G. Cao, S. Garroni, D. Bellucci, V. Cannillo, Synthesis, sintering, mechanical properties, and oxidation behavior of $(Zr_{0.5}Me_{0.5})B_2$ (Me = Ta, Hf) solid solutions, Ceram. Int. 50 (7) (2024) 12158–12166, https://doi.org/10.1016/j.ceramint.2024.01.119.

[23] S. Barbarossa, A.M. Locci, G. Cao, S. Garroni, A. Balbo, F. Zanotto, E. Sani, R. Orrù, Processing and optical behavior of dense $(Hf,Zr)B_2$ solid solutions for solar energy receivers, Sol. Energy Mater. Sol. Cells 268 (2024) 112755, https://doi.org/10.1016/j.solmat.2024.112755.

[24] E. Pakhomova, G. Cao, R. Orrù, S. Garroni, P. Ferro, R. Licheri, High-entropy diborides—silicon carbide composites by reactive and non-reactive spark plasma sintering: a comparative study, Materials 17 (3) (2024) 718, https://doi.org/10.3390/ma17030718.

[25] M. Casu, S. Barbarossa, A.M. Locci, G. Cao, C. Cau, L. Caggiu, S. Garroni, P. Ferro, R. Orrù, Processing and characterization of ultra high temperature high-entropy $(Ti_{0.2}Zr_{0.2}Hf_{0.2}Mo_{0.2}W_{0.2})B_2$-based ceramics: effect of W granulometry, graphite, and SiC addition, J. Alloy. Compd. 1007 (2024) 176492, https://doi.org/10.1016/j.jallcom.2024.176492.

[26] Z.A. Munir, U. Anselmi-Tamburini, M. Ohyanagi, The effect of electric field and pressure on the synthesis and consolidation of materials: a review of the spark plasma sintering method, J. Mater. Sci. 41 (2006) 763–777, https://doi.org/10.1007/s10853-006-6555-2.

[27] S. Grasso, Y. Sakka, G. Maizza, Pressure effects on temperature distribution during spark plasma sintering with graphite sample, Mater. Trans. 50 (8) (2009) 2111–2114, https://doi.org/10.2320/matertrans.M2009148.

[28] L. Lutterotti, R. Ceccato, R. Dal Maschio, E. Pagani, Quantitative analysis of silicate glass in ceramic materials by the Rietveld method, Mater. Sci. Forum 87 (1998) 278–281, https://doi.org/10.4028/www.scientific.net/MSF.278-281.87.

[29] W.G. Fahrenholtz, J. Binner, J. Zou, Synthesis of ultra-refractory transition metal diboride compounds, J. Mater. Res. 31 (18) (2016) 2757–2772, https://doi.org/10.1557/jmr.2016.210.

[30] R.G. Munro, Material properties of titanium diboride, J. Res. Natl. Inst. Stand. Technol. 105 (2000) 709–720, https://doi.org/10.6028/jres.105.057.

[31] W. Oliver, G. Pharr, An improved technique for determining hardness and elastic modulus using load and displacement sensing indentation experiments, J. Mater. Res. 7 (1992) 1564–1583, https://doi.org/10.1557/JMR.1992.1564.

[32] C.B. Ponton, R.D. Rawlings, Vickers indentation fracture toughness test. Part 1: review of literature and formulation of standardised indentation toughness equations, Mater. Sci. Technol. 5 (1989) 865–872, https://doi.org/10.1179/mst.1989.5.9.865.

[33] C.B. Ponton, R.D. Rawlings, Vickers indentation fracture tough-ness test. Part 2: application and critical evaluation of standardised indentation toughness equations, Mater. Sci. Technol. 5 (1989) 961–976, https://doi.org/10.1179/mst.1989.5.10.961.

[34] I. Barin, Thermochemical Data of Pure Substances, VHC, Weinheim, Germany, 1989.
[35] C. Musa, R. Orrù, D. Sciti, L. Silvestroni, G. Cao, Synthesis, consolidation and characterization of monolithic and SiC whiskers reinforced HfB_2 ceramics, J. Eur. Ceram. Soc. 33 (2013) 603–614, https://doi.org/10.1016/j.jeurceramsoc.2012.10.004.
[36] B. Huang, S. Chen, Z. Yao, M. Zhang, Y. Jing, B. Li, W. Xiong, Study of carbothermal synthesis of TiB_2 assisted by extended high-energy milling, Powder Technol. 275 (2015) 69–76, https://doi.org/10.1016/j.powtec.2014.12.025.
[37] F. Monteverde, F. Saraga, M. Gaboardi, Compositional disorder and sintering of entropy stabilized (Hf,Nb,Ta,Ti,Zr)B_2 solid solution powders, J. Eur. Ceram. Soc. 40 (12) (2020) 3807–3814, https://doi.org/10.1016/j.jeurceramsoc.2020.04.026.
[38] M.M. Opeka, I.G. Talmy, E.J. Wuchina, J.A. Zaykoski, S.J. Causey, Mechanical, thermal, and oxidation properties of hafnium and zirconium compounds, J. Eur. Ceram. Soc. 19 (13-14) (1999) 2405–2414, https://doi.org/10.1016/s0955-2219(99)00129-6.
[39] W.G. Fahrenholtz, G.E. Hilmas, I.G. Talmy, J.A. Zaykoski, Refractory diborides of zirconium and hafnium, J. Am. Ceram. Soc. 90 (5) (2007) 1347–1364, https://doi.org/10.1111/j.1551-2916.2007.01583.x.
[40] B. Basu, G.B. Raju, A.K. Suri, Processing and properties of monolithic TiB2 based materials, Int. Mater. Rev. 51 (6) (2006) 352–374, https://doi.org/10.1179/174328006X102529.
[41] J. Ma, Y. Du, M. Wu, G. Li, Z. Feng, M. Guo, Y. Sun, W. Song, M. Lin, X. Guo, A simple inorganic-solvent-thermal route to nanocrystalline niobium diboride, J. Alloy. Compd. 468 (1-2) (2009) 473–476, https://doi.org/10.1016/j.jallcom.2008.01.021.
[42] C. Nico, T. Monteiro, M.P.F. Graça, Niobium oxides and niobates physical properties: review and prospects, Prog. Mater. Sci. 80 (2016) 1–37, https://doi.org/10.1016/j.pmatsci.2016.02.001.
[43] K.J. Griffith, A. Senyshyn, C.P. Grey, Structural stability from crystallographic shear in TiO_2-Nb_2O_5 phases: cation ordering and lithiation behavior of $TiNb_{24}O_{62}$, Inorg. Chem. 56 (7) (2017) 4002–4010, https://doi.org/10.1021/acs.inorgchem.6b03154.
[44] C. Liu, P. Luo, Y. Feng, W. Gong, F. Zhang, Phase equilibria in the TiO_2–Nb_2O_5 system: new experiments and thermodynamic modelling, Ceram. Int. 49 (18) (2023) 30471–30480, https://doi.org/10.1016/j.ceramint.2023.06.311.
[45] A. Herklotz, K.M. Grove, M.S. Bowen, R.M. Quade, K.E. Tippey, D.P. Cann, Insights into the $Hf_nNb_2O_{2n+5}$ homologous phases from experimental, first-principle, and force-field studies, J. Am. Ceram. Soc. 107 (10) (2024) 6554–6561, https://doi.org/10.1111/jace.19949.